

Modified Quaternary Nanostructure on Graphene sheets as Counter electrode for Dye-sensitized Solar Cells

Yonrapach Areerob^a, Won-Chun Oh^{a, b*}

^aDepartment of Advanced Materials Science & Engineering, Hanseo University, Chungnam 356-706, South Korea

^bCollege of Materials Science and Engineering, Anhui University of Science & Technology, Huainan 232001, PR China

Abstract: The dye-sensitized solar cell (DSSC) plays a leading role in third generation photovoltaic devices. Platinum-loaded conducting glass has been widely exploited as the standard counter electrode (CE) for DSSCs. However, the high cost and the rarity of platinum limits its practical application in DSSCs. This has promoted large interest in exploring Pt-free CEs for DSSCs. Very recently, graphene, which is an atomic planar sheet of hexagonally arrayed sp² carbon atoms, has been demonstrated to be a promising CE material for DSSCs due to its excellent conductivity and high electrocatalytic activity. This article provides a mini review of graphene-based CEs for DSSCs. Firstly, the fabrication and performance of graphene film CE in DSSCs are discussed. Secondly, DSSC counter electrodes made from graphene-based quaternary composite materials are evaluated. Finally, a brief outlook is provided on the future development of graphene-based materials as prospective counter electrodes for DSSCs.

Keyword: Graphene, Quaternary Material, DSSC, Counter electrode

Introduction

Dye-sensitized solar cells (DSSCs) have attracted much attention and have been extensively studied since their discovery by Graetzel et al [1]. In recent years, the efficiency of DSSC has reached up to 12.3% [2]. Given their various advantages, such as simplicity, eco-friendly fabrication, and low cost, DSSC have emerged to be one of the most promising alternatives to conventional silicon-based solar cells [3-6]. DSSC comprises two electrodes separated by an electrolyte containing an iodide/tri-iodide redox couple: a dye-attached nanocrystalline TiO₂ film on a fluorine-doped tin oxide (FTO) glass as the anode and a Pt counter electrode as the cathode. The counter electrode transfers electrons from the external circuit back to the electrolyte and simultaneously catalyzes the reduction of I₃⁻ to I⁻ ions. The light reflection and scattering by the counter electrode can increase the light absorption efficiency of the photoanode. Therefore, the counter electrode structure that exhibits high catalyzing activity and excellent optical characteristics could achieve more efficient DSSCs.

Different counter electrode structures have been widely investigated recently and different fabrication processes of Pt coating have been developed. The most representative Pt coating processes used to fabricate counter electrodes for DSSC include electrochemical deposition and thermal treatment, electron-beam evaporation, sputtering, thermal decomposition of H_2PtCl_6 , and self-assembly of Pt nanoparticles [8–11]. Counter electrodes have also been fabricated from other materials such as carbon black, carbon nanotubes [12], graphene [13,14], and various polymers [15–17]. DSSCs with Pt counter electrodes have higher energy-conversion efficiency compared with other DSSCs as the Pt has excellent electrocatalytic performance, chemical and thermal stability, and strong light reflection [18]. Recent studies about Pt counter electrodes show that electrodes with rough surface or micro-nanostructure can increase the contact area of Pt/electrolyte interface and thereby improving the performance of DSSCs [19–21], however, these reported methods are limited by the cumbersome prepare processes and uncontrollable morphology.

In illustrates a schematic of classical DSSC configuration with operational principle. As the heart of a DSSC, mesoscopic semiconductor oxide layer having a percolating network of anatase TiO_2 nanoparticles should be sintered to establish electronic conduction and to adhere to fluorine-doped tin oxide (FTO) or indium-doped tin oxide (ITO) layer, yielding a film thickness of ca. 10 nm and a porosity of 50–60%. This mesoporous TiO_2 layer is sensitized by a monolayer of photosensitive dye molecules. When exposed to sunlight, complicated charge-transfer processes are created in a DSSC, allowing for converting solar energy into electricity. Under persistent irradiation by incident light, the organic dye molecules can absorb photons, elevate their energy level from ground to their excited state, and release electrons to conduction band of anatase TiO_2 . The photogenerated electrons will transfer along the percolating network of TiO_2 nanoparticles to FTO layer and then flow to CE across the external load, whereas the oxidized dye is regenerated to its original state by I^- ions. The I_3^- ions formed by oxidation of I^- diffuse a short distance (<50nm) through the electrolyte layer to the CE, where the regenerative cycle is completed by electron transfer to reduce I_3^- back to I^- species. A robust CE must be catalytically active for accelerating reaction and efficiently reduce the overpotential. The overpotential is required to drive the reaction at a certain current density, which gives rise to a charge-transfer resistance (Rct). A Rct of < 1 $\Omega \text{ cm}^2$ is a prerequisite to avoid significant electron loss during transfer processes, therefore, the design and synthesis of novel Pt-free or low-Pt CEs is still on the way.

2. EXPERIMENTAL

2.1 Preparation of quaternary nanostructure for counter electrodes

The quaternary composite based counter electrodes were prepared by hot injection method [22]. The as-deposited precursor films were annealed at different annealing temperatures, times, ramping rates and in different atmospheres. The CZTS thin film substrates were loaded in a quartz tube furnace. For an N_2 atmosphere where different

annealing temperature, time and ramping rate conditions were applied, the tube was evacuated using a rotary vacuum pump and the furnace tube subsequently filled with N₂ gas. For a H₂S atmosphere, after rotary pump evacuation, a gas mix of H₂S and N₂ with a composition ratio of 20:80 was introduced at a pressure of 0.15 atm. For furnace annealing treatments, various temperatures, times and ramping rates were applied. The processes commenced at 300 °C with a ramping rate of 10 °C/min for 1 hour under N₂ atmosphere. After that the furnace was left to cool slowly overnight.

2.2 Preparation of Graphene materials

GO was synthesized by a modified Hummers' method. In summary, 13 mL concentrated H₃PO₄ and 120 mL concentrated H₂SO₄ were mixed and 1 g graphite was added to the solution, then 6 g KMnO₄ was added slowly to the solution. The mixture was heated to 50 °C under stirring for 24 h and then added to 130 mL ice bath with 1 mL of H₂O₂ (30%). The mixture turned to orange in this step. It was centrifuged at 4000 rpm for 2 h and the sediment phase was washed by water, HCl (30%) and ethanol (99%), respectively. The product was dried at 60 °C to obtain GO.

2.3 Fabrication of DSSCs

The DSSCs were fabricated by injecting iodide electrolyte solution between dye sensitized TiO₂ photoanodes and quaternary metal based counter electrodes. Iodide electrolyte solution with high redox potential was composed of 0.3 M of LiI, 0.03 M of I and 1:1 solvent mixture of acetonitrile and tert-butyl alcohol. For electrochemical impedance (EIS) measurements, the symmetrical dummy cells were constructed by two identical counter electrodes (CE/electrolyte/ CE) and the electrolyte is similar to the one used for DSSC fabrication.

3. RESULTS AND DISCUSSION

3.1 DSSC counter electrodes

As shown in **Fig. 1**, a typical dye-sensitized solar cell consists of a dye-sensitized nanocrystalline TiO₂ film as the photoanode, a counter electrode (CE) and an electrolyte with a redox couple in the liquid or solid state [22-24]. The CE's task is to reduce redox species in liquid solar cells, which are used as mediators in the regeneration of the sensitizer after electron injection, or to collect holes from the hole conducting material in solid-state DSSCs. For an optimized cell, one must choose a CE material with the lowest possible sheet resistance, excellent catalytic activity for the reduction of the redox electrolyte, high chemical stability and a low cost. The reactions at the CE are dependent on the type of redox mediator used to transfer charge between the photoelectrode and the CE. In most cases, the iodide-tri-iodide couple has been employed as the redox mediator and the overall redox reaction in DSSCs can be described as:

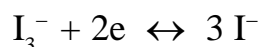


Figure Caption

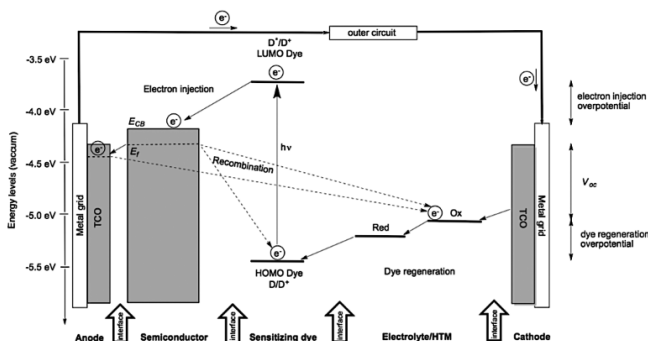


Fig. 1. A schematic of a DSSC in principle.

The tri-iodides are produced near the dye-sensitized TiO₂ electrode and reduced at the counter electrode. Platinum-loaded conducting glass has been widely employed as the standard CE for DSSCs due to its high catalytic activity and excellent conductivity as well as its high corrosion stability against iodine in the electrolyte [25–27]. However, the combination between the limited resource of platinum and the large application of platinum-based catalysts in the vehicle industry makes platinum extremely expensive and in diminishing supply. Therefore, it is important to explore Pt-free materials to replace the Pt counter electrode for DSSCs [28]. For this reason, recent attention has been focused on various materials as potential alternatives to Pt, including carbon, [29–31] transition metal sulfides, [32–35] nitrides [36–38] and carbides.

Kay and Gratzel first explored a graphite/carbon black mixture as a counter electrode [39] due to its low cost and abundance. This pioneering work stimulated intensive research to evaluate various types of carbon for DSSC counter electrodes. It was reported that, under AM 1.5 simulated sunlight, energy conversion efficiencies were 6.67, 3.9, 4.5 and 7.7% for DSSCs with counter electrodes of graphite, [40] activated carbon, [41] single-walled carbon nanotubes (SWCNTs) [43] and multi-walled carbon nanotubes (MWCNTs), [42] respectively. Furthermore, DSSC with large-effective surface-area polyaromatic hydrocarbon (LPAH) counter electrodes achieved an energy conversion efficiency of 7.89%. [44] Currently, the main drawback of carbon-based counter electrodes is the requirement of a large amount of carbon to reach comparable efficiencies to Pt-based CEs. This makes the device bulkier and more opaque. [45] As a rising star in the carbon family, graphene, with its unique properties, is being explored as a DSSC counter electrode to solve these issues.

3.2 Graphene-based counter electrodes for DSSCs

Graphene was expected to be a promising material for DSSC counter electrodes due to its excellent conductivity that can decrease charge transfer resistance (R_{ct}). Kaniyoor and Ramaprabhu showed that the R_{ct} of thermally exfoliated graphene (TEG) films is 11.7 Ω cm², which is very close to that of Pt electrodes (6.5 Ω cm²). The DSSCs fabricated

with TEG as a counter electrode exhibited a power conversion efficiency of about 2.8%, comparable to that (about 3.4%) of Pt-based DSSCs. Furthermore, Zhang et al. [46] made similar observations, namely, the R_{ct} value of graphene nanosheet (GN) films is close to that of Pt, resulting in comparable efficiencies between the DSSCs using GNs and Pt as counter electrodes. So far, several groups have explored graphene-based counter electrodes. [47-51] From Table 1, one can see that the reported efficiencies of DSSCs fabricated with graphene counter electrodes vary from 0.7 to 6.8%. The difference in the efficiency with graphene counter electrodes is mainly due to the utilization of different techniques for the graphene film preparation and the DSSC fabrication. Graphene films for DSSC counter electrodes have been formed by various techniques, including thermal exfoliation from graphite oxide, [52] the oxidative exfoliation of graphite followed by hydrazine reduction, the chemical reduction of graphene oxide colloids under microwave irradiation [51] and electrophoretic deposition (EPD) followed by an annealing treatment. So far, the best DSSC efficiency (6.8%) has been obtained with a graphene counter electrode fabricated via the following approach: [53] graphene nanosheets (GN), which were synthesized by a hydrazine reduction of exfoliated graphene oxide, were ground in a terpeneol solution and then deposited on a FTO glass, followed by annealing in air. It was shown that the annealing temperature used for the GN-based counter electrode exhibited a remarkable effect on the performance of DSSCs, namely, the PV performance increased and then dropped with an increasing annealing temperature. The optimized annealing temperature was 400 °C, at which the best performance was achieved. The best cell showed a short-circuit current (JSC) of 17 mA cm⁻², an open-circuit voltage (VOC) of 0.747 V and a fill factor (FF) of 53.62% under the illumination of 100 mW cm⁻², leading to a high energy conversion efficiency of 6.8%. It was found that there was a trade-off between enhancing the adhesion and increasing the electrical conductivity of the GN film on the FTO glass by the annealing treatment in air. When the annealing temperature was higher than 400 °C, the GN film was easier to peel off from the substrate due to the presence of fewer organic binders (terpeneol and ethyl cellulose), which were burned out at high temperatures, causing a higher R_{ct} in the counter electrode.

The performance of a DSSC with a graphene counter electrode is dependent on the structure of graphene. Perfect graphene has an extremely high conductivity, but it may possess a limited number of active sites for I_3^-/I^- electrocatalysis. Kavan et al. demonstrated that the electrocatalytic activity of graphene nanosheets is usually associated with its defects and oxygen-containing functional groups. [54] It is well known that lattice surface defects exist in graphene sheets prepared from graphite via an oxidation- reduction approach. Lattice defects are considered as electro- catalytic active sites. On the other hand, Roy-Mayhew et al. found that increasing the number of oxygen-containing functional groups in a graphene sheet enhanced its electrocatalytic activity for I_3^- reduction. [55] Furthermore, Xu et al. reported that reduced graphene oxide (RGO) functionalized with -NHCO- groups exhibited a higher catalytic ability than the original RGO. [56] This indicates that -NHCO- groups can increase catalytic activity. However, it is still unclear what specific oxygen-containing functional groups

in the RGO sheets are mainly responsible for the I_3^- / I^- electrocatalysis. In addition, it was found that the DSSC with the counter electrode, which was made from partially reduced graphene oxide, exhibited a low conversion efficiency equal to 40% that of a Pt-based cell. [57] This happened because the partially reduced graphene oxide had too many oxygen-containing groups, which decreased the electrical conductivity of graphene. [58] Therefore, one must make a balance between the electrical conductivity and the electrocatalytic activity of graphene to optimize the DSSC by functionalization.

3.3 Graphene/metal composites

A strategy to reduce Pt loading in DSSCs is to exploit Pt/graphene composite materials as counter electrodes. [59] Gong et al. synthesized a Pt/graphene composite (Fig. 2(a)) via the self-assembly of polyelectrolyte, graphene and H_2PtCl_6 , followed by an annealing treatment. [60] The DSSC with the Pt/graphene composite as a counter electrode achieved a power conversion efficiency of 7.66%, comparable to that (8.16%) of the DSSC with a sputtered-Pt counter electrode. Importantly, the Pt/graphene counter electrode contained much less Pt than the sputtered-Pt electrode, leading to a dramatic decrease in the DSSC fabrication cost. Furthermore, the effect of Pt loading on the PV performance of the DSSCs was evaluated by Bajai et al. [61] They deposited Pt nanoparticles on graphene layers using a pulsed laser ablation method (Fig. 2b) and revealed that the amount of Pt loading had a remarkable influence on the efficiency of the resulting DSSCs. An optimized Pt loading (27.43%) was obtained. The DSSC with the optimized Pt/graphene counter electrode not only contained a lower amount of Pt, but it also exhibited an improved conversion efficiency. The efficiency improvement was attributed to the increase in the graphene sheet defects caused by Pt as the D/G ratio of the Raman spectra (Fig. 3) was increased by incorporating Pt into the graphene sheets. [61]

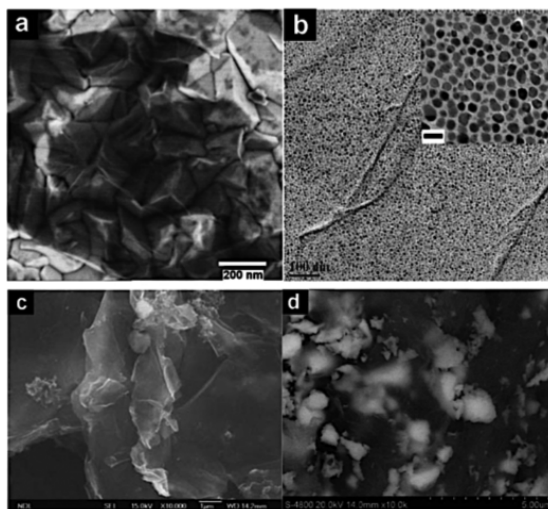


Fig. 2. SEM images of (a) the FTO/graphene/Pt counter electrode, [59] (b) the graphene/Pt composite, [60] (c) the graphene/Pt composite [61] and (d) the graphene/ $Ni_{12}P_5$ composite. [62]

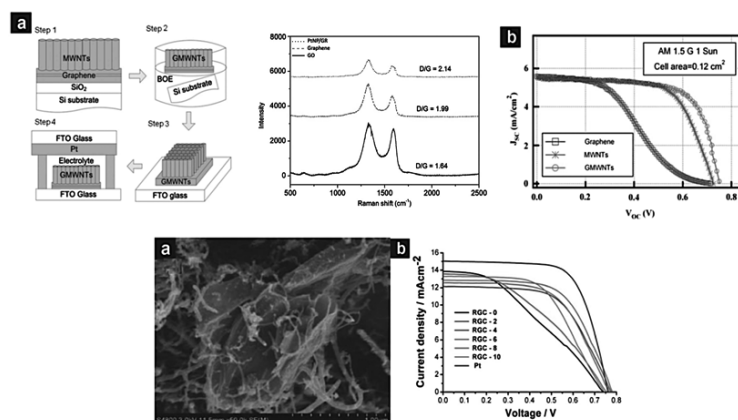


Fig. 3. (a) A schematic diagram, Synthesis of G-MWCNTs on SiO₂/Si, (2) the lift-off process of G-MWCNTs, (3) the transplant to FTO glass, (4) half the cell without TiO₂ and dye) and (b) the J-V characteristics of DSSCs with different counter electrodes: graphene, MWCNTs and G-MWCNTs. Raman spectra of GO, graphene and PtNP/GR with the corresponding D/G ratios [62]. (a) An FE-SEM image of RGC-6 and (b) J-V curves of DSSCs with various graphene/CNTs counter electrodes (where the CNT contents are 0, 20, 40, 60, 80 and 100% for RGC-0, RGC-2, RGC-4, RGC-6, RGC-8 and RGC-10, respectively).

Ni was also combined with graphene to form composite counter electrodes. Dou et al. employed a hydrothermal reaction for the synthesis of Ni₁₂P₅/graphene composites, in which Ni₁₂P₅ nanoparticles were embedded into the graphene sheets (Fig. 2d). Furthermore, they demonstrated that the Ni₁₂P₅/graphene exhibited excellent electrocatalytic activity for I₃⁻ reduction, resulting in a high efficiency (5.7%) for the DSSC with the Ni₁₂P₅/graphene counter electrode (Table 1).

Table 1 PV characteristics of DSSCs fabricated with graphene counter electrodes

	Jsc (mA cm ⁻²)	Voc (V)	FF (%)	PCE (%)
Graphene	7.70	0.68	0.54	2.82
Graphene	16.98	0.74	0.53	6.81
Graphene	6.12	0.64	0.56	2.19
Graphene	5.60	0.70	0.60	2.30
Graphene	14.30	0.54	0.65	5.69
Graphene	8.11	0.72	0.46	2.64
Graphene	6.42	0.70	0.16	0.74

The role of graphene in these metal/graphene composite materials was recognized as a scaffold to well disperse metal (Pt or Ni₁₂P₅) particles, increasing the availability of the metal particles for electron transfer.

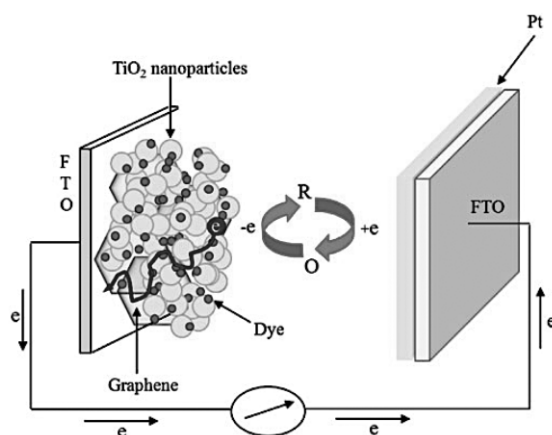


Fig. 4. An illustration of the electrochemical reaction process in graphene/metal composites.

[62] Furthermore, graphene could also provide a fast diffusion pathway for the electrolyte and ensure excellent electrode–electrolyte contact, which improves the electron transfer rate at the interface. The metal (Pt or Ni_{12}P_5) nanoparticle can serve as both the active site for electrocatalytic processes and the spacer between the graphene sheets to accelerate the diffusion of the electrolyte (Fig. 4).

3.4 Quaternary composites

(a) $\text{Cu}_2\text{ZnSnS}_4$

Quaternary chalcogenides such as $\text{Cu}_2\text{ZnSnS}_4$, $\text{Cu}_2\text{ZnSnS}_4$ (CFTS) and other related chemical compounds are of great interest when considering renewable energy. CFTS is environmentally benign and cheap to fabricate because of the abundance of elements such as Cu, Fe, Sn, and S in nature. The valence states of Cu(I), Fe(II), and Sn(IV) have been established to be 2 : 1 : 1 : 4 in atomic ratio, and various solid solution⁵ using CFTS was synthesized and investigated several years ago. Therefore, we can reduce the cost of production by utilizing natural resources on earth compared to In, Ga of $\text{Cu}(\text{In}_x\text{Ga}_{1-x})\text{Se}_2$ (CIGS) and continue to exploit sufficient underground reserves of iron [63].

Likewise, there are other plausible materials as an alternative catalyst, including carbon materials, [64] PEDOT related materials, [65] PPy (polypyrrole), [66] graphene, [67] sulfur-doped nickel oxide, CoS, and CZTSSe. [68-69] Recently, chalcogenide based counter electrodes (CEs) are emerging due to facileness to prepare at relatively low temperature compared to graphene based CEs and low fabrication cost resulting from the abundance of elements such as Cu, Fe, and S in nature. In CZTSSe, the power conversion efficiency is comparable to that of Pt when the material was spin cast and selenized. Thus we fabricated DSSC using many different chalcogenide compounds such as CuS, Cu_2S , SnS_2 , CuSnS_3 , Cu_2SnS_4 , $\text{Cu}_2\text{ZnSnS}_4$, and $\text{Cu}_2\text{FeSnS}_4$, as counter electrodes. Of those, the efficiency of the DSSC with $\text{Cu}_2\text{FeSnS}_4$ was the best. Also, among CFTSs with tetragonal, wurtzite, and zinc blende¹ crystal structures, we have focused on stannite CFTS with zinc blende.

As shown in Fig. 5(a), the XRD pattern of the prepared CFTS nanoparticles indicates that they are in a zinc blende phase without any impurities such as FeS_2 , Cu_2S , CuFeS_2 , or Cu_3SnS_4 , with most intense peaks at $2\theta = 28.5^\circ$, 47.2° , 47.6° , and 56.1° corresponding to (112), (220), (204), and (312) planes. The mean crystallite size diameter (D) of nanoparticles can be calculated based on the XRD spectra by Scherrer's formula. In Fig. 5(b), the calculated sizes from full-width at half maximum (FWHM) are about 34 nm in diameter. It might be due to aggregation of CFTS after annealing at 400°C for 15 min. [70]

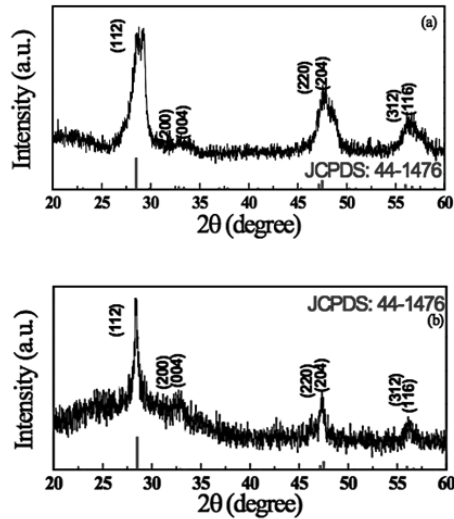


Fig. 5. (a) XRD pattern of as-prepared CFTS nanoparticles, (b) XRD pattern of CFTS thin film on FTO glass. [70]

TEM images in Fig. 6 (a, b) show that the size of CFTS nanoparticles is 11 to 15 nm and the CFTS nanoparticles are round shaped, well-dispersed, and uniform. The selected area electron diffraction pattern in Fig. 6 (c) matches the zinc blende coordinated structure of CFTS, as indicated by the diffraction spots corresponding to the (112), (004), (204), and (116) planes. After annealing, the sizes of CFTS nanoparticles are about in the range of 30–40 nm as shown in the SEM image in Fig. 7(a, b). Fig. 7(c) shows the cross sectional image of CFTS coated on FTO glass, the thickness of CFTS particles ranges from 70 to 150 nm thick. By using nonpolar solvent such as toluene, the CFTS nanoparticles were well dispersed. The spin coating condition was optimized with 1000 rpm for 20 s. [71] The spin coating was repeated for 7 times in order to obtain the optimum film thickness and in turn better catalytic effect as shown in the cyclic voltammogram (see Fig. 8).

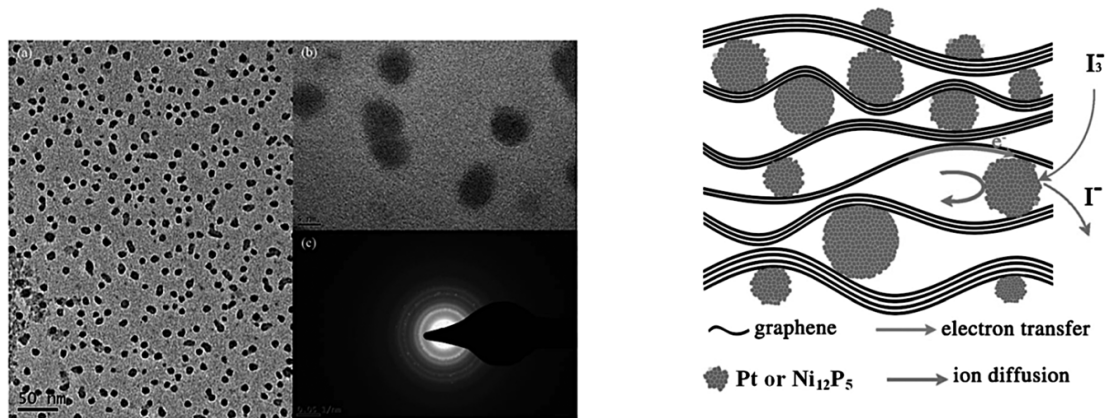


Fig. 6. (a) TEM and (b) HRTEM images of zinc blende CFTS nanoparticles. (c) SAED pattern of CFTS. An illustration of the electrochemical reaction process in graphene/metal composites. [71-72]

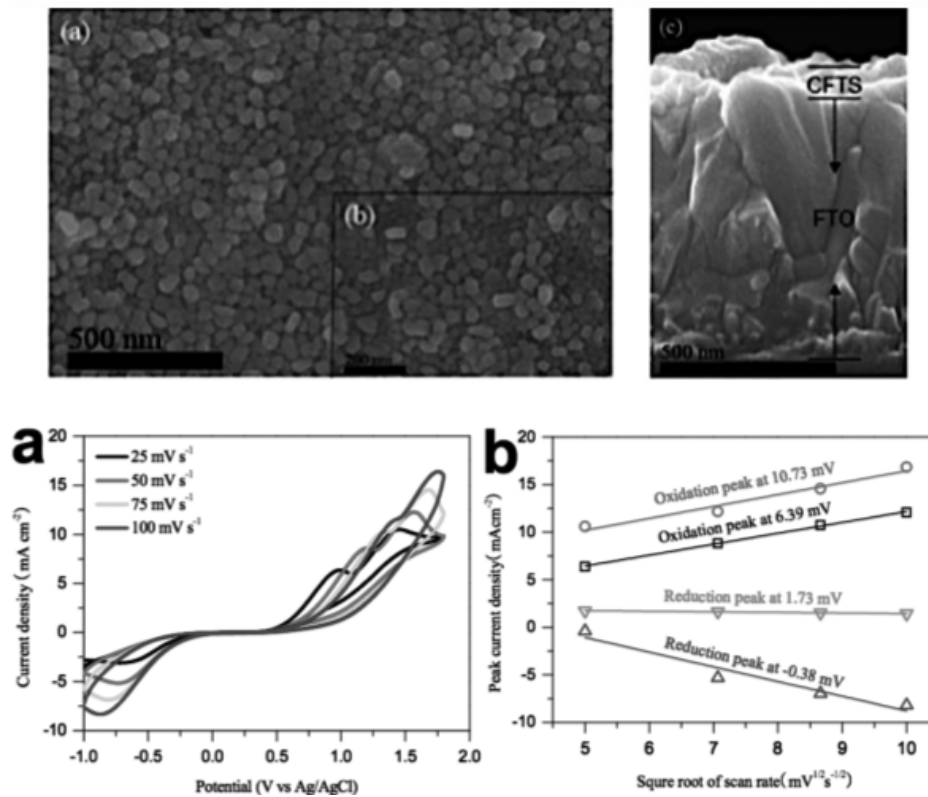


Fig. 7. (a) FE-SEM images and (b) magnified top images of CFTS on a FTO glass. (c) Cross sectional image of CFTS on a FTO glass. [73]

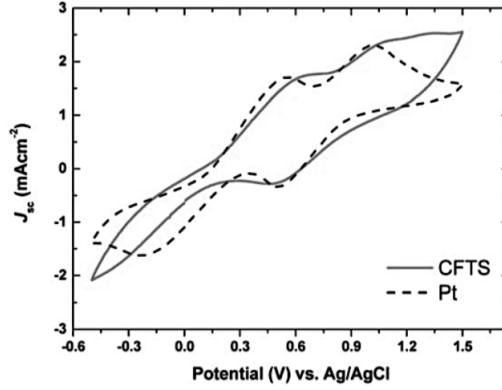


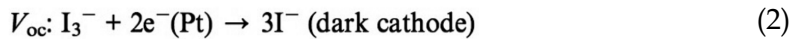
Fig. 8. Cyclic voltammogram of CFTS and Pt. [74]

Cell performance of CFTS and Pt is shown in Fig. 9 and Table 2. Photovoltaic performances with each counter electrode are quite comparable to each other except the Voc value.

Table 2. Photovoltaic data on Pt and CFTS based DSSC, respectively

	J _{sc} (mA cm ⁻²)	V _{oc} (V)	FF (%)	PCE (%)
Pt	12.9	0.77	71.3	7.1
CFTS	13.4	0.64	64.3	5.6
CuS	9.5	0.62	26.1	1.5
Cu ₂ S	17.4	0.44	21.2	1.6
SnS ₂	11.4	0.65	32.0	2.4
CuSnSeS ₃	12.8	0.66	43.3	3.6
CuSnSeS ₄	12.9	0.65	38.5	3.2
CZTS	10.7	0.66	56.9	4.0

$$V_{oc} = \left(\frac{kT}{e} \right) \ln \left(\frac{l_{inj}}{n_{cb} k_{et} [I_3^{-1}]} \right) \quad (1)$$



where k is the Boltzmann constant, T is the absolute temperature, e is the electric charge, I_{inj} is the incident photo flux, n_{cb} is the concentration of electrons at the TiO_2 surface, and k_{et} is the rate constant for the back-electron-transfer reaction.

As per the eqn (1) and (2), an open circuit voltage (V_{oc}) of the cell depends on the concentration of I_3^{-} ions present in the electrolyte system. When compared to the Pt based conventional counter electrode, lower catalytic effect of CFTS material showed lesser degree of reduction of I_3^{-} ions into $3I^{-}$ ions. Thus the lower performance of CFTS electrode showed higher concentration of I_3^{-} ions than that of the Pt based counter electrode. The higher concentration of I_3^{-} ions leads to the V_{oc} drop as per the eqn (1).

In the case of conventional Pt counter electrode, the reduction process is more effective thus the leaving behind the lower concentration of I_3^- ions in turn higher V_{oc} value was obtained. From the cyclic voltammogram, the lower cathodic current was observed in the region of 0.3 to 0.2 V for CFTS electrode which infers the lower cathodic performance and also causes the V_{oc} drop. [72-75]

From the J-V curve (see **Fig. 9**), there is an increasing trend of fill factor has been observed for the CuS and CuSnS₃ type materials depending on the valence state of the copper cations. For example, CuS and CuSnS₃ having +2 valence state of copper ion shows higher fill factor value than the Cu₂S and Cu₂SnS₄ having lower valence (+1) state of copper ions. The higher fill factor of CuS and CuSnS₃ may be due to the more positive valence state of copper ion which causes good bonding tendency towards the anionic counterpart and in turn the whole compound is chemically more stable than the Cu₂S and Cu₂SnS₄. [76]

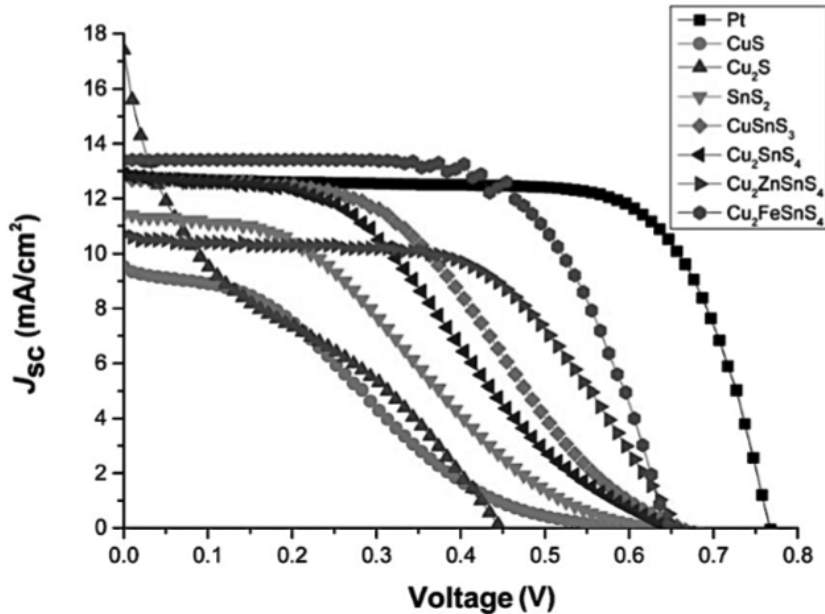


Fig. 9. J-V curve of DSSC with CFTS and Pt using iodine electrolyte under AM 1.5 illumination, respectively.

Also, CFTS type DSSC shows a lower fill factor value than that of Pt type DSSC. In order to understand the reason, electro-chemical impedance spectroscopy (EIS) analysis was done to characterize the cell resistance as shown in **Fig. 10**. The noticeable semiarc which is the first semiarc (R_{ct1}) indicates that the resistances at the interface of counter electrode/electrolyte in a CFTS type DSSC (0.16 W) is slightly smaller than that of a Pt type DSSC (0.24 W). [76-78] This is because a CFTS type DSSC has a smaller resistance at the above interface than a Pt type DSSC. This chalcogenide EIS data which indicated a small R_{ct1} in SnS nanosheets type DSSC was recently demonstrated in a SnSx counter electrode based DSSC paper.

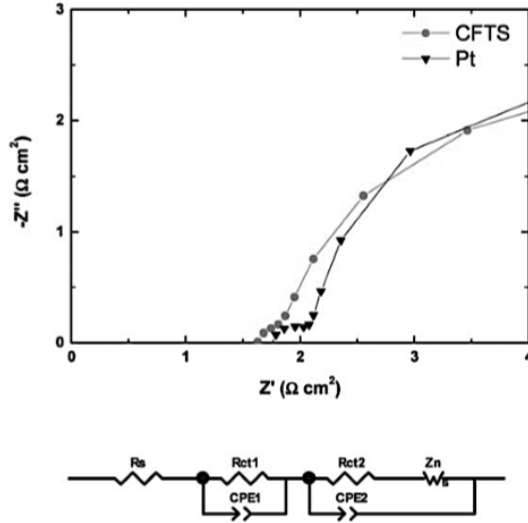


Fig. 10. Electrochemical impedance spectra of DSSC with CFTS and Pt using iodine electrolyte under AM 1.5 illumination.

(b) Graphene-Bi₅FeTi₃O₁₅ (BFTO)

Bi₅FeTi₃O₁₅ (BFTO) is a member of perovskite family, which exhibits a variety of interesting physical properties containing magnetic, ferroelectric, and dielectric properties. BFTO is a kind of material with a direct bandgap (2.13 eV), high chemical stability and non-toxicity. BFTO can be gained by inserting BiFeO₃ into three-layered Bi₄Ti₃O₁₂, forming a four-layered perovskite structure. Bi₄Ti₃O₁₂ and BiFeO₃ have been found to be good candidates for DSSC. [77] As a result, BFTO could also be utilized to build DSSCs. However, these ferroelectric oxides as CE in DSSC have scarcely been reported. In this work, we demonstrated BFTO/Gr nanocomposites as CE in DSSCs due to the low charge mobility and inferior catalytic activity of BFTO CE, expecting that Gr could promote the catalytic activity of the nanocomposites CE and thus enhance the photovoltaic property of the DSSCs based on the BFTO. This work could widen the potential applications of multi basic oxides in the photo physics and photochemistry field.

Fig. 11 presents the XRD patterns of pure BFTO nanofibers, Gr powders, and BGr nanocomposites, respectively. The positions and relative intensities of diffraction peaks are corresponding to JCPDS card NO.38-1257 and 65-6212, which indicate that the BFTO and Gr are pure phase within the limitation of XRD diffractometer, respectively. [78] Moreover, the UV-vis spectra of the BFTO, BGr, and Gr. According to the spectrum of BFTO, it could find that BFTO absorbs light from UV light to visible light shorter than 600 nm, which is consistent with its yellow appearance. According to the UV-vis spectra, the Gr has a perfect photo absorption property in the whole visible light region. Therefore,

BFTO compounded with Gr could display a better light-harvesting capability over the visible to near-IR region, which is also ascertained by the UV-vis spectra of BGr nanocomposites.

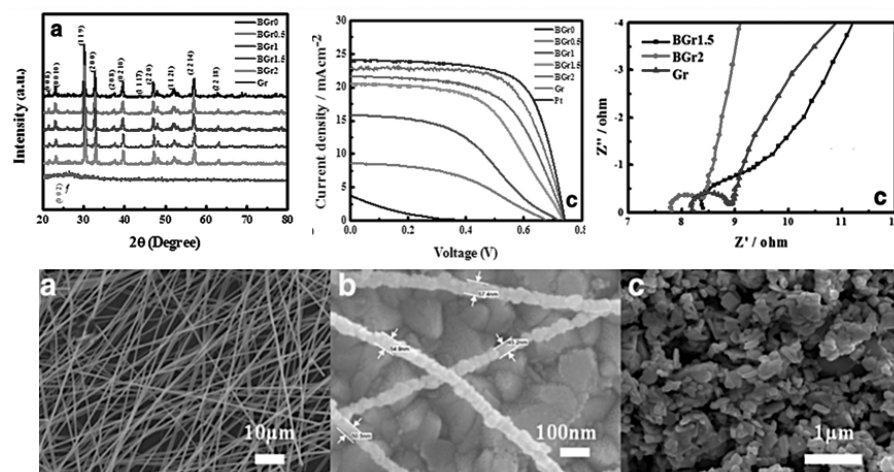


Fig.11. XRD patterns of the BFTO, BGr, and Gr, Current density-voltage curves (J-V), EIS measurement and Representative SEM images of uncentered nanofibers.

EIS measurement is performed in symmetrical cells fabricated with two identical CEs (CE/electrolyte/CE) to analyze the correlation between the electrocatalytic activity of the CE and quality of devices. The intercept on the horizontal axis stands for the series resistance (R_s), a reflection of conductive substrate resistance, and lead resistance. The charge transfer resistance (R_{ct}) at the CE/electrolyte interface is the intercept of the first semicircle, which characterizes the electrocatalytic ability of CEs for the reduction of triiodide, while the Nernst diffusion impedance corresponding to the diffusion resistance of the redox couples in the electrolyte is referred by the second arc. It is worthwhile to note that R_{ct} and R_s are the important parameters for appraising the performance of CEs. It is well known that a smaller R_s represents a higher conductivity and the smaller R_{ct} , the lower ΔE_p , bringing about a faster electron transfer from CE to electrolyte, thus the electrocatalytic activity can be enhanced. The J-V curves for the DSSCs fabricated with various CEs are shown in Fig. 11c, and the detailed photovoltaic parameters estimated from the J-V curves, including open-circuit voltage (V_{oc}), short-circuit current density (J_{sc}), fill factor (FF). The photovoltaic parameters of DSSCs are gradually eased with increasing Gr content. When the mass fraction of Gr exceeds 2%, the PCE of DSSC remains nearly constant based on numerous photoelectric performance measurements. It is found that the DSSC assembled by BGr2 gives a PCE of 9.56%, V_{oc} of 740 mV, J_{sc} of 21.56 mA/cm², and FF of 0.599, which is forty times greater than that of the DSSC based on the pristine BFTO CE (PCE = 0.22%, V_{oc} = 0.364 V, J_{sc} = 3.8 mA/cm², and FF = 0.159). Consequently, Gr can advance the electrocatalytic activity of the

BFTO CE which is in line with the former tests (EIS and Tafel curves). The improved photovoltaic performance of the DSSCs after Gr incorporation mainly ascribes to the following aspects: The contact frequency between the redox couple in electrolyte and the electrode can be accelerated owing to the large specific surface area of Gr, thus improve the electrolyte absorption ability and reaction speed. Then, the BGr CEs exhibit an improved electrocatalytic activity and electrolyte/electrode contact area compared with that of pure BFTO CE, leading to fast reaction kinetics and offering more electrocatalytic sites for the reduction of I_3^- at the CE/electrolyte and a low charge recombination. Our study clearly demonstrates that small amount of Gr can significantly improve the electrochemical and photovoltaic properties of BFTO.

3.5 Prospects and challenges

Although some Pt alloy CE catalysts with advanced nanostructures have shown remarkable activity and enhanced dissolution-resistance in I^- / I_3^- redox electrolyte, the low retention of active catalyst nanostructure during DSSC operation environmental is still a remaining issue. For example, the crystal facets that contain more catalytically active sites could be converted to a low active facet due to thermodynamic environmental changes in the DSSC. Other aspects in the future work should be considered: (i) optimizing the geometry, composition and structure of alloy CE catalysts to further improve their catalytic activity and stability; (ii) analyzing the potential mechanisms from theoretical calculation and work functions of the alloy CEs; (iii) further exploring new catalyst morphologies by new strategies to resolve the issue of low retention in highly active nanostructures; (iv) developing more cost-effective but efficient Pt-free alloy CEs to meet the requirements for DSSC commercialization; (v) enhancing the oxidation resistance of transition metal species in alloy CEs by rational structural and morphologies designs; (vi) integrating low-Pt or Pt-free alloy electrocatalysts with carbonaceous materials or conductive polymers.

4. CONCLUSION

In this article, we have summarized the recent studies of the CEs with carbonaceous materials and conductive polymers along with advances in Pt and alloy CE systems for DSSC applications. The development of solution synthesis with peculiar nanostructures and versatile behaviors has enabled systematic studies of Pt-based and Pt-free alloys for electrocatalytic applications. Critical parameters such as particle size, shape, and composition are believed to have significant effects on catalytic activity enhancement. These studies as well as structural optimization may eventually lead to advanced CE catalysts suitable for highly efficient but cost-effective DSSCs. Even though the study on alloy CEs is at a primary stage, the impressive photovoltaic performances and cost-effectiveness have demonstrated it is a feasible strategy of elevating solar-to-electric efficiency and reducing cost of electricity generation. However, we still have many aspects to be considered before realizing the cost effective electricity generation from DSSCs. This critical review represents an important step forward, as it demonstrates how to make the CEs active and stable as well as to enhance electrocatalytic activity and to

reduce fabrication cost for high-efficiency DSSC platforms.

Reference

1. K. Saranya, M. Rameez, A. Subramania, *Eur. Polym. J.* 66 (2015) 207.
2. W.C. Oh, K.Y. Cho, C.H. Jung, Y. Areerob, *J. Photochem. Photobiol., A* 2019, 372, 11–20.
3. A.G. Kannan, J.X. Zhao, S.G. Jo, Y.S. Kang, D.W. Kim, *J. Mater. Chem. A* 2 (2014) 12232.
4. Y. Areerob, J.Y. Cho, W.K. Jang, K.Y. Cho, W.C. Oh, *Solid state Ionic* 2018, 327, 99–109
5. S.-J. Ha and J. H. Moon, *Sci. Rep.*, 2014, 4, 5375.
6. S. K. Deb, *Renewable Energy*, 1996, 8, 375–379.
7. K. L. Chopra, P. D. Paulson and V. Dutta, *Prog. Photovolt: Res. Appl.*, 2004, 12, 69–92.
8. S.H. Park, H.R. Jung, W.J. Lee, *Electrochim. Acta* 102 (2013) 423.
9. X. Sheng, L. Shen, T. Kim, L. Li, X. Wang, R. Dowdy, P. Froeter, K. Shigeta, X. Li, R. G. Nuzzo, N. C. Giebink and J. A. Rogers, *Adv. Energy Mater.*, 2013, 3, 991– 996.
10. Y. Areerob, K.Y. Cho, C.H. Jung, W.C. Oh, *J Alloys Compd* 2019, 775, 690–697.
11. H. Lin, Irfan, W. Xia, H. N. Wu, Y. Gao and C. W. Tang, *Sol. Energy Mater. Sol. Cells*, 2012, 99, 349–355.
12. D.Y. Kang, Y. Lee, C.Y. Cho, J.H. Moon, *Langmuir* 28 (2012) 7033.
13. D.W. Zhang, X.D. Li, H.B. Li, S. Chen, Z. Sun, X.J. Yin, S.M. Huang, *Carbon* 49 (2011) 5382.
14. Y. Areerob, K.Y. Cho, W.C. Oh, *New J. Chem.* 41, 2017, 9613–9622.
15. J. B. Li, V. Chawla and B. M. Clemens, *Adv. Mater.*, 2012, 24, 720–723.
16. G. Nobile and M. Morana, in *Solar Energy Materials and Solar Cells*, 2003, vol. 76, pp. 511–520.
17. D.S. Yu, E. Nagelli, F. Du, L.M. Dai, *J. Phys. Chem. Lett.* 1 (2010) 2165.
18. R. Hussein, D. Borchert, G. Grabosch and W. R. Fahrner, *Sol. Energy Mater. Sol. Cells*, 2001, 69, 123–129.
19. L. Shen, F. Meng and Z. Liu, *Sol. Energy*, 2013, 97, 168–175.
20. S. Ito, H. Miura, S. Uchida, M. Takata, K. Sumioka, P. Liska, P. Comte, P. Pechy and M. Gratzel, *Chem. Commun.*, 2008, 5194–5196.
21. M. R. Narayan, *Renewable Sustainable Energy Rev.*, 2011, 16, 208–215.
22. M. R. Kim and D. Ma, *J. Phys. Chem. Lett.*, 2015, 6, 85–99.
23. H. Liu, J. Tang, I. J. Kramer, R. Debnath, G. I. Koleilat, X. Wang, A. Fisher, R. Li, L. Brzozowski, L. Levina and E. H. Sargent, *Adv. Mater.*, 2011, 23, 3832–3837.
25. M. C. Scharber and N. S. Sariciftci, *Prog. Polym. Sci.*, 2013, 38, 1929–1940.
26. S. Kazim, M. K. Nazeeruddin, M. Gratzel and S. Ahmad, *Angew. Chem., Int. Ed.*, 2014, 53, 2812–2824.
27. M. Saliba, T. Matsui, J.-Y. Seo, K. Domanski, J.-P. Correa-Baena, M. K. Nazeeruddin, S. M. Zakeeruddin, W. Tress, A. Abate, A. Hagfeldt and M. Gratzel, *Energy Environ. Sci.*, 2016, 9, 1989–1997.
28. E. M. Sanehira, A. R. Marshall, J. A. Christians, S. P. Harvey, P. N. Ciesielski, L. M. Wheeler, P. Schulz, L. Y. Lin, M. C. Beard and J. M. Luther, *Sci. Adv.*, 2017, 3, 4204.
29. K. Kakiage, Y. Aoyama, T. Yano, K. Oya, J. Fujisawa and M. Hanaya, *Chem. Commun.*, 2015, 51, 15894–15897.
31. Dye Sensitized Solar Cells (DSSC/DSC) 2013–2023, [https:// www.idtechex.com/research/reports/dye-sensitized-solar-cells-dssc-dsc-2013-2023-technologies-markets-players-000345.asp](https://www.idtechex.com/research/reports/dye-sensitized-solar-cells-dssc-dsc-2013-2023-technologies-markets-players-000345.asp).
32. B. O'Regan and M. Gratzel, *Nature*, 1991, 353, 737.

33. M. K. Nazeeruddin, A. Kay, I. Rodicio, R. Humphry-Baker, E. Mueller, P. Liska, N. Vlachopoulos and M. Graetzel, *J. Am. Chem. Soc.*, 1993, 115, 6382–6390.
34. J. Wu, Z. Lan, J. Lin, M. Huang, Y. Huang, L. Fan and G. Luo, *Chem. Rev.*, 2015, 115, 2136–2173.
35. W. Feng, Y. Li, J. Du, W. Wang and X. Zhong, *J. Mater. Chem. A*, 2016, 4, 1461–1468.
36. G. Calogero, A. Bartolotta, G. Di Marco, A. Di Carlo and F. Bonaccorso, *Chem. Soc. Rev.*, 2015, 44, 3244–3294.
37. A. A. Mohamad, *J. Power Sources*, 2016, 329, 57–71.
39. M. Suzuka, N. Hayashi, T. Sekiguchi, K. Sumioka, M. Takata, N. Hayo, H. Ikeda, K. Oyaizu and H. Nishide, *Sci. Rep.*, 2016, 6, 28022.
40. F. Cao, G. Oskam and P. C. Searson, *J. Phys. Chem.*, 1995, 99, 17071–17073.
41. H. Rensmo, K. Keis, H. Lindstrom, S. Sodergren, A. Solbrand, A. Hagfeldt, S.-E. Lindquist, L. N. Wang and M. Muhammed, *J. Phys. Chem. B*, 1997, 101, 2598–2601.
42. U. Bach, D. Lupo, P. Comte, J. E. Moser, F. Weissortel, J. Salbeck, H. Spreitzer and M. Gratzel, *Nature*, 1998, 395, 583–585.
43. M. K. Nazeeruddin, P. Peichy, T. Renouard, S. M. Zakeeruddin, R. Humphry-Baker, P. Cointe, P. Liska, L. Cevey, E. Costa, V. Shklover, L. Spiccia, G. B. Deacon, C. A. Bignozzi and M. Gratzel, *J. Am. Chem. Soc.*, 2001, 123, 1613–1624.
44. F. Gao, Y. Wang, D. Shi, J. Zhang, M. Wang, X. Jing, R. Humphry-Baker, P. Wang, S. M. Zakeeruddin and M. Gratzel, *J. Am. Chem. Soc.*, 2008, 130, 10720–10728.
45. Q.J. Yu, Y.H. Wang, Z.H. Yi, N.N. Zu, J. Zhang, M. Zhang and P. Wang, *ACS Nano*, 2010, 4, 6032–6038.
46. T. Horiuchi, H. Miura and S. Uchida, *J. Photochem. Photobiol., A*, 2004, 164, 29–32.
47. S. Kim, J. K. Lee, S. O. Kang, J. Ko, J. H. Yum, S. Fantacci, F. DeAngelis, D. DiCenso, M. K. Nazeeruddin and M. Gratzel, *J. Am. Chem. Soc.*, 2006, 128, 16701–16707.
48. A. Kay and M. Graetzel, *J. Phys. Chem.*, 1993, 97, 6272–6277.
49. S. Mathew, A. Yella, P. Gao, R. Humphry-Baker, B. F. Curchod, N. Ashari-Astani, I. Tavernelli, U. Rothlisberger, N. Khaja and M. Gratzel, *Nat. Chem.*, 2014, 6, 242–247.
50. M. K. Nazeeruddin, R. Humphry-Baker, D. L. Officer, W. M. Campbell, A. K. Burrell and M. Gratzel, *Langmuir*, 2004, 20, 6514–6517.
51. K. Kakiage, M. Yamamura, E. Fujimura, T. Kyomen, M. Unno and M. Hanaya, *Chem. Lett.*, 2010, 39, 260–262.
52. K. Kakiage, Y. Aoyama, T. Yano, T. Otsuka, T. Kyomen, M. Unno and M. Hanaya, *Chem. Commun.*, 2014, 50, 6379–6381.
53. M. Lv, D. Zheng, M. Ye, J. Xiao, W. Guo, Y. Lai, L. Sun, C. Lin and J. Zuo, *Energy Environ. Sci.*, 2013, 6, 1615–1622.
54. W. Zhang, Y. Xie, D. Xiong, X. Zeng, Z. Li, M. Wang, Y.-B. Cheng, W. Chen, K. Yan and S. Yang, *ACS Appl. Mater. Interfaces*, 2014, 6, 9698–9704.
55. Y. Yang, J. Zhao, C. Cui, Y. Zhang, H. Hu, L. Xu, J. Pan, C. Li and W. Tang, *Electrochim. Acta*, 2016, 196, 348–356.
56. A. M. Bakhshayesh, M. R. Mohammadi, H. Dadar and D. J. Fray, *Electrochim. Acta*, 2013, 90, 302–308.
57. E. J. W. Crossland, N. Noel, V. Sivaram, T. Leijtens, J. A. Alexander-Webber and H. J. Snaith, *Nature*, 2013, 495, 215–219.
58. T. S. Bhat, S. S. Mali, S. D. Korade, J. S. Shaikh, M. M. Karanjkar, C. K. Hong, J. H. Kim and P. S. Patil, *J. Mater. Sci.: Mater. Electron.*, 2017, 28, 304–316.
59. W. Wang, H. Zhang, R. Wang, M. Feng and Y. Chen, *Nanoscale*, 2014, 6, 2390–2396.
60. J. Xu, G. Wang, J. Fan, B. Liu, S. Cao and J. Yu, *J. Power*

Sources, 2015, 274, 77–84.

61. J. De Peng, P. C. Shih, H. H. Lin, C. M. Tseng, R. Vittal, V. Suryanarayanan and K. C. Ho, *Nano Energy*, 2014, 10, 212–221.
62. F. Du, B. Yang, X. Zuo and G. Li, *Mater. Lett.*, 2015, 158, 424–427.
63. A. Birkel, Y.-G. Lee, D. Koll, X. Van Meerbeek, S. Frank, M. J. Choi, Y. S. Kang, K. Char and W. Tremel, *Energy Environ. Sci.*, 2012, 5, 5392–5400.
64. D. K. Pawar, J. S. Shaikh, B. S. Pawar, S. M. Pawar, P. S. Patil and S. S. Kolekar, *J. Porous Mater.*, 2012, 9, 649–655.
65. R. C. Pawar, J. S. Shaikh, P. S. Shewale and P. S. Patil, *J. Alloys Compd.*, 2011, 509, 1716–1721.
66. R. C. Pawar, J. S. Shaikh, S. S. Suryavanshi and P. S. Patil, *Curr. Appl. Phys.*, 2012, 12, 778–783.
67. R. C. Pawar, J. S. Shaikh, N. L. Tarwal, M. M. Karanjkar and P. S. Patil, *J. Mater. Sci.: Mater. Electron.*, 2012, 23, 349–355.
68. R. C. Pawar, J. S. Shaikh and P. S. Patil, *Mater. Today*, 2011, 14, 447.
69. R. C. Pawar, J. S. Shaikh, A. A. Babar, P. M. Dhere and P. S. Patil, *Sol. Energy*, 2011, 85, 1119–1127.
70. R. C. Pawar, J. S. Shaikh, A. V. Moholkar, S. M. Pawar, J. H. Kim, J. Y. Patil, S. S. Suryavanshi and P. S. Patil, *Sens. Actuators, B*, 2010, 151, 212–218.
71. S. H. Mujawar, A. I. Inamdar, C. A. Betty, R. Cerc Korosec and P. S. Patil, *J. Appl. Electrochem.*, 2011, 41, 397–403.
72. R. Ghosh, M. K. Brennaman, T. Uher, M.-R. Ok, E. T. Samulski, L. E. McNeil, T. J. Meyer and R. Lopez, *ACS Appl. Mater. Interfaces*, 2011, 3, 3929–3935.
73. H.-N. Kim and J. H. Moon, *ACS Appl. Mater. Interfaces*, 2012, 4, 5821–5825.
74. P. S. Patil, S. H. Mujawar, A. I. Inamdar, P. S. Shinde, H. P. Deshmukh and S. B. Sadale, *Appl. Surf. Sci.*, 2005, 252, 1643–1650.
75. M. M. Rashad and A. E. Shalan, *Appl. Phys. A*, 2013, 116, 781–788.
76. J. K. Sharma, M. S. Akhtar, S. Ameen, P. Srivastava and G. Singh, *J. Alloys Compd.*, 2015, 632, 321–325.
77. E. Guo and L. Yin, *Phys. Chem. Chem. Phys.*, 2015, 17, 563–574.
78. R. Sahay, J. Sundaramurthy, P. Suresh Kumar, V. Thavasi, S. G. Mhaisalkar and S. Ramakrishna, *J. Solid State Chem.*, 2012, 186, 261–267.



This document was created with the Win2PDF "print to PDF" printer available at <http://www.win2pdf.com>

This version of Win2PDF 10 is for evaluation and non-commercial use only.

This page will not be added after purchasing Win2PDF.

<http://www.win2pdf.com/purchase/>